



HAL
open science

One-step synthesis of Cu_xO_y/TiO_2 photocatalysts by laser pyrolysis for selective ethylene production from propionic acid degradation

Juliette Karpriel, Pierre Lonchambon, Frédéric Dappozze, Ileana Florea, Diana Dragoie, Chantal Guillard, Nathalie Herlin-Boime

► To cite this version:

Juliette Karpriel, Pierre Lonchambon, Frédéric Dappozze, Ileana Florea, Diana Dragoie, et al.. One-step synthesis of Cu_xO_y/TiO_2 photocatalysts by laser pyrolysis for selective ethylene production from propionic acid degradation. *Nanomaterials*, 2023, 13 (5), pp.792. 10.3390/nano13050792. hal-04301846

HAL Id: hal-04301846

<https://hal.science/hal-04301846>

Submitted on 23 Nov 2023

HAL is a multi-disciplinary open access archive for the deposit and dissemination of scientific research documents, whether they are published or not. The documents may come from teaching and research institutions in France or abroad, or from public or private research centers.

L'archive ouverte pluridisciplinaire **HAL**, est destinée au dépôt et à la diffusion de documents scientifiques de niveau recherche, publiés ou non, émanant des établissements d'enseignement et de recherche français ou étrangers, des laboratoires publics ou privés.

1 Communication

2 One-step synthesis of $\text{Cu}_x\text{O}_y/\text{TiO}_2$ photocatalysts by laser py- 3 rolysis for selective ethylene production from propionic acid 4 degradation

5 Juliette Karpriel ^{1,2}, Pierre Lonchambon ¹, Frédéric Dappozze ², Ileana Florea ³, Diana Dragoie ⁴, Chantal Guillard ^{2,*},
6 Nathalie Herlin-Boime ^{1,*}

7 ¹ NIMBE, CEA, CNRS, Université Paris-Saclay, CEA Saclay 91191 Gif-sur-Yvette, France

8 ² Université Lyon 1, Institut De Recherche Sur La Catalyse Et l'Environnement De Lyon (IRCELYON), CNRS,
9 Avenue Albert Einstein, 69626, Villeurbanne, France

10 ³ Laboratory of Physics of Interfaces and Thin Films (LPICM), Ecole Polytechnique, CNRS, Institut Polytech-
11 nique de Paris, Palaiseau 91128, France

12 ⁴ Université Paris-Saclay, CNRS, Institut de Chimie Moléculaire et des Matériaux d'Orsay (ICMMO), F-91405
13 Orsay, France

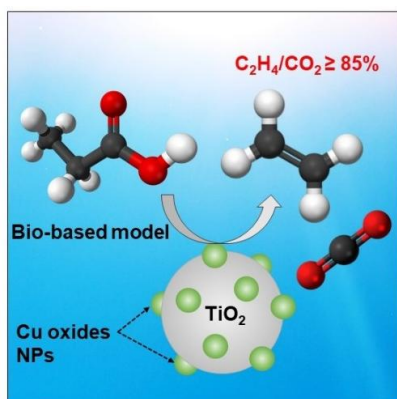
14 * Correspondence: nathalie.herlin@cea.fr; chantal.guillard@ircelyon.univ-lyon1.fr
15

16

17

Abstract: In an effort to produce alkenes in an energy-saving way, this study presents for the first time a photocatalytic process that allows obtaining ethylene with high selectivity from propionic acid (PA) degradation. To this end, TiO_2 nanoparticles (NPs) modified with copper oxides ($\text{Cu}_x\text{O}_y/\text{TiO}_2$) were synthesized by laser pyrolysis. The atmosphere of synthesis (He or Ar) strongly affects the morphology of photocatalysts and therefore their selectivity towards hydrocarbons (C_2H_4 , C_2H_6 , C_4H_{10}) and H_2 products. Specifically, $\text{Cu}_x\text{O}_y/\text{TiO}_2$ elaborated under He environment presents highly dispersed copper species and favors the production of C_2H_6 and H_2 . On the contrary, $\text{Cu}_x\text{O}_y/\text{TiO}_2$ synthesized under Ar involves copper oxides organized into distinct NPs of ~2 nm diameter and promotes C_2H_4 as the major hydrocarbon product, with a selectivity *i.e.* $\text{C}_2\text{H}_4/\text{CO}_2$ as high as 85% versus 1% obtained with pure TiO_2 .

Keywords: photocatalysis; ethylene; hydrocarbons; hydrogen; titanium dioxide; propionic acid



27

28

Citation: To be added by editorial staff during production.

Academic Editor: Firstname
Lastname

Received: date

Revised: date

Accepted: date

Published: date



Copyright: © 2023 by the authors.

Submitted for possible open access

publication under the terms and

conditions of the Creative Commons

Attribution (CC BY) license

(<https://creativecommons.org/licenses/by/4.0/>).

1. Introduction

Ethylene (C_2H_4) is a key molecule in chemical industry. About 75% of petrochemical products are obtained from this light olefin, including intermediates like ethylene glycol and polymers such as polyethylene or polyvinyl chloride [1–3]. Currently, ethylene is mostly produced from the steam cracking of fossil fuels. However, besides relying on non-sustainable feedstock and being extremely polluting, such method is one of the most energy-consuming processes in the chemical sector as it requires considerable working temperatures ($T > 750^\circ\text{C}$) [4,5].

Hence, researchers are developing new strategies for a cleaner and lower-cost ethylene production without the use of hydrocarbons. Among them, heterogeneous photocatalysis attracts great attention for being an oxidation process operating at ambient temperature and atmospheric pressure, thus offering favorable perspectives for sustainable organic synthesis using solar light [6]. Nonetheless, very few research articles describe the photocatalytic production of ethylene. Despite its high relevance, CO_2 photocatalytic reduction to C_2H_4 is very challenging as it requires effective C-C coupling and multi-electron reaction process [7]. Another strategy to form ethylene consists on the

45 photocatalysis of carboxylic acids, operating in an anaerobic media. Pho-
46 to-decarboxylation of such acids (acetic, propionic, butanoic etc.) mainly produces CO₂,
47 H₂ and alkanes [8–13], using TiO₂ or TiO₂-based nanomaterials decorated with metal
48 co-catalysts to promote quantum yield maximization [14]. In some cases, alkenes were
49 also detected. Kraeutler and Bard [11] identified ethylene traces from propionic acid de-
50 carboxylation with Pt/TiO₂ which will be confirmed afterwards in Betts *et al* study using
51 TiO₂ P25 [12]. Scandura *et al* enhanced propene and ethylene selectivities respectively
52 from butyric acid and propionic acid photoreforming with Au/TiO₂ compared to Pt/TiO₂
53 [10]. However, despite the use of onerous noble metals, alkenes were each time detected
54 in trace amounts.

55 Herein, we report for the first time the selective photocatalytic production of eth-
56 ylene from the valorization of propionic acid using TiO₂ modified with copper nanopar-
57 ticles under UVA light. Specifically, TiO₂ and Cu_xO_y/TiO₂ photocatalysts were elaborated
58 by laser pyrolysis technique, an industrial-scale process that enables a one-step and con-
59 tinuous synthesis of nanopowders at several grams per hour. The impact of laser pyrol-
60 ysis operating atmosphere (Ar, He) on the morphology and the materials photocatalytic
61 performances were studied. Propionic acid (PA) was selected as model molecule - this
62 volatile fatty acid can be obtained from fermentation of organic wastes [15]. This work
63 provides a new method for sustainable ethylene production with low energy consump-
64 tion and low-cost photocatalysts.

65 2. Materials and Methods

66 2.1. Chemicals

67 Titanium (IV) isopropoxide (TTIP, ≥ 97% purity), ethylacetate (99.8% purity) and
68 copper (II) acetylacetonate (Cu(acac)₂, ≥ 97% purity) were purchased from Sig-
69 ma-Aldrich. Pure o-xylene was supplied from Fisher. Helium He, argon Ar and ethylene
70 C₂H₄ gases were supplied by Air Products. All the reactants were used without further
71 purification. Propionic acid (PA) was obtained from Sigma-Aldrich (≥ 99.5% purity).
72

73 2.2. Chemicals Synthesis of TiO₂ and Cu_xO_y/TiO₂ nanoparticles

74 The synthesis of TiO₂ and Cu modified TiO₂ photocatalysts was performed with the
75 laser pyrolysis technique under He or Ar gas. This method permits the continuous and
76 direct production of nanopowders, and is described elsewhere [16]. Briefly, its principle
77 is based on the orthogonal interaction of an infrared CO₂ laser (10.6 μm) in continuous
78 mode with a gaseous or liquid mixture of reagents. The laser was focused by the mean of
79 a cylindrical lens, resulting in a horizontal beam of about 30 mm. For the synthesis of
80 reference samples (TiO₂), the mixture consisted on 175 g of liquid titanium (IV)
81 isopropoxide (TTIP) dissolved in a 150 mL o-xylene/ethylacetate solution (65 vol%/35
82 vol%). Dissolution of 4.13 g of Cu(acac)₂ (copper (II) acetylacetonate) into the previous
83 mixture permitted to obtain Cu_xO_y/TiO₂ particles with a theoretical Cu content equals to
84 2.0 wt% regarding final nanomaterials. The resulting liquid was converted into
85 microdroplets with a spray generator regulating the mixture at 30°C. The liquid droplets
86 were transported into the reactor zone through a carrier gas (He or Ar) at 2 000 cm³.min⁻¹
87 flow. A sensitizer gas (C₂H₄, 800 cm³.min⁻¹) was added to the carrier gas to enhance the
88 laser absorption of the precursors. The reaction zone was confined by He or Ar inert gas
89 flow. The CO₂ laser power (measured under inert gas) was set to 670 W and the pressure
90 inside the reactor was regulated to 740 Torr. The powders were collected on filters lo-
91 cated downstream.

92 The TiO₂ and Cu_xO_y/TiO₂ as-formed materials had the appearance of black, grey or
93 brown coloured powders due to the presence of carbon impurities. All samples were
94 further annealed under air at 450°C during 6 hours in a tubular furnace (Carbolite) to
95 remove residual carbon. The annealed particles were labelled TiO₂-X and Cu/TiO₂-X (X =

He, Ar) depending on their synthesis environment. Powders images are provided in Figure S.1.

2.3. Samples characterization

The morphology of prepared photocatalysts was evaluated by Transmission Electron Microscopy (TEM, Fei Tecnai G2 F20).

In order to probe the presence of Cu element, Energy-Dispersive Spectroscopy (EDS) analyses have been performed in the Scanning Transmission Electron Microscope High-Angle Annular Dark Field (STEM-HAADF) imaging mode of a 200 kV Titan-Themis TEM/STEM electron microscope equipped with a Cs probe corrector and a ChemiSTEM Super-X detector. These two accessories allow chemical mapping of light and heavy elements with a spatial resolution in the picometer range. The experimental conditions were set so that the total current within the probe used for the STEM-HAADF EDS chemical analysis was about 85 pA.

Samples specific surface areas were determined by N₂ adsorption according to Brunauer-Emmett-Teller (BET) method with a Micromeritics 3Flex apparatus. Briefly, BET method is based on the measurement of the N₂ gas molecules physisorption onto the solid sample.

Crystalline phases were identified by X-Ray Diffraction (XRD) measurements using a Bruker D2 Phaser diffractometer with monochromatized Cu K α radiation ($\lambda = 1.5418 \text{ \AA}$). Anatase (JCPDS No. 21-1272) and rutile (JCPDS No. 21-1276) percentages were calculated from Spurr and Myers equation [17].

XPS measurements were performed on a K-Alpha spectrometer from ThermoFisher, equipped with a monochromated X-ray Source (Al K α , 1486.7 eV) with a spot size of 400 μm . The hemispherical analyser was operated in CAE (Constant Analyser Energy) mode, with a pass energy of 200 eV and a step of 1 eV for the acquisition of surveys spectra and a pass energy of 50 eV and 10 eV and a step of 0.1 eV for the acquisition of narrow scans. The spectra were recorded and treated by means of Avantage software. The binding energy scale was calibrated against the Ti 2p binding energy set a 258.5 eV.

Copper content was measured by Inductively Coupled Plasma Optical Emission Spectroscopy (ICP-OES) with a Horiba Jobin Yvon Activa instrument. Carbon content was determined by using a Horiba Ema-320V Carbon/Sulphur analyzer.

2.4. Photocatalytic measurements

Photocatalytic runs were carried in a 250 mL Pyrex photoreactor equipped with a mechanic agitator (500 rpm), a gas inlet and outlet for gas sampling and purge. A 18W PL-L Phillips lamp, placed below the photoreactor, was chosen as the UVA source with a UV band of 350-410 nm centered at 370 nm (irradiance of 5 mW.cm⁻²).

100 mL of a 1.0 vol% PA solution containing 50 mg of photocatalyst was introduced into the reactor. A continuous flow of argon (70 mL.min⁻¹) was applied through a bubbler for 6 hours into the system to fully remove the ambient air. After the purge, the photoreactor was sealed and irradiated with UVA light. Every 65 min, a 2 mL aliquot of photoproduct gases in the headspace were carried by vacuum pumping into a Clarus 500 GC FID-PDHID for analysis. Products were firstly separated through a RT-Q-Bond (Restek - 30 m x 0.53 mm x 20 μm) column before FID with Polyarc methanization module. For PDHID, a RT-M5A molecular sieve (Restek - 30 m x 0.32 mm x 30 μm) was added. Carrier gas was helium N60 grade (Messer). For each gaseous analysis, the oven temperature was set at 50°C rising at 20°C/min to reach a maximum temperature of 150°C maintained for additional 55 min. Tests were repeated twice to ensure reproducibility.

3. Results and discussion

3.1. Physico-chemical properties

3.1.1. Synthesis

During the laser pyrolysis synthesis, the flame observed under Ar atmosphere was more intense than under He atmosphere, indicating a higher flame temperature and leading to a more efficient decomposition of precursors. It is possible to observe the flame during synthesis experiment through a window. The flame seen in presence of helium is much less bright than under argon, which is an indication of a lower flame temperature under He atmosphere. The temperature appears to be a major parameter due to the change of atmosphere. Specific heat capacity of helium is 10 times higher than argon, explaining such a lower temperature reached in helium atmosphere after laser absorption as well as fast temperature decrease. As a consequence, the lower temperature observed under He atmosphere explains a lower grain size as well as a lower rutile content in nanoparticles synthesized under He compared to nanoparticles generated under Ar (Table 1 and Figure 1). Similar observations were reported by Pignon *et al* [16], who explained these results as a cooling effect of He as well as less efficient confinement of the reactants. Indeed, He is a light gas and is therefore less efficient to confine the reaction. This is also apparent from the lower production rate (*i.e.* collected powder, Table 1) in He compared to Ar.

Table 1 summarizes the characteristics of the obtained $\text{Cu}_x\text{O}_y/\text{TiO}_2$ samples and their TiO_2 references synthesized in similar conditions. In agreement with the more efficient decomposition of precursors, production rate is higher under Ar atmosphere and carbon content increases in the as formed TiO_2 -Ar and Cu/TiO_2 -Ar samples compared to samples obtained under He environment.

After annealing, TiO_2 samples turned white indicating the efficient removal of carbon species whereas $\text{Cu}_x\text{O}_y/\text{TiO}_2$ powders appeared pale green-coloured, suggesting the presence of copper. The associated mass losses are in agreement with the carbon content of the as formed powders. This result is confirmed with elementary analyses revealing only traces of residual carbon ≤ 0.3 wt% in all the samples.

Table 1. Characteristics of TiO_2 and $\text{Cu}_x\text{O}_y/\text{TiO}_2$ elaborated under He and Ar atmospheres (unless

Samples	Production rate (g/h)	C content before annealing (wt%)	Mass loss after annealing (%)	BET surface area ($\text{m}^2\cdot\text{g}^{-1}$) (diameter ^a (nm))	TEM diameter ^b (nm)	Crystallinity (phase fraction)		Cu content (wt%)
						Anatase	Rutile	
TiO_2 -He	5.1	34.5	41	111 (13.6)	15 ± 4	87%	13%	-
TiO_2 -Ar	10.3	44.7	49	81 (18.6)	16 ± 6	76%	24%	-
Cu/TiO_2 -He	4.5	17.9	22	138 (10.8)	12 ± 3	89%	11%	1.76 ± 0.04
Cu/TiO_2 -Ar	9.5	53.9	58	40 (35.7)	31 ± 11	53%	47%	1.91 ± 0.04

specified, characterization results concern annealed powders).

^a Calculated from $6000/\text{specific surface area (Brunauer-Emmett-Teller - BET) } [\text{m}^2\cdot\text{g}^{-1}] \times \text{density } [\text{g}/\text{cm}^3]$ formula. Density takes into account anatase and rutile proportions determined by XRD as well as Cu content measured by ICP-OES.

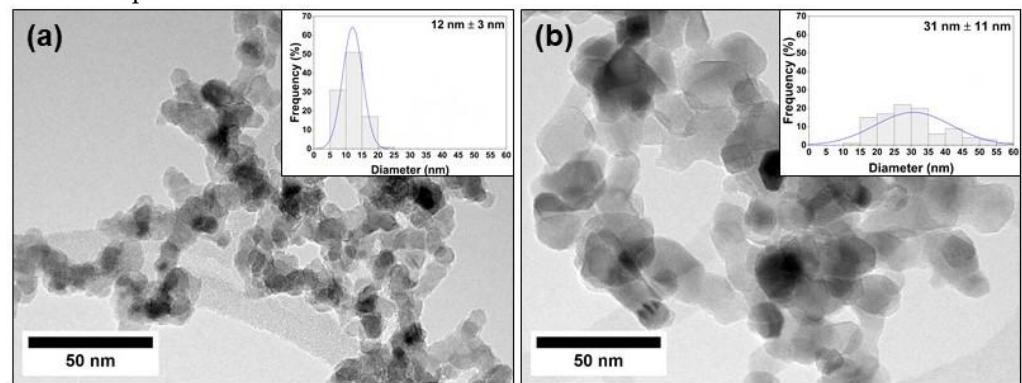
^b Diameter estimated from the measure of 100 particles using ImageJ software.

3.1.2. Morphology and structure

The morphology of the annealed samples was first investigated by TEM analysis (Figure 1 and Figure S.2). From the TEM images, all particles appear to present mostly a spherical shape arranged in chains typical of gas phase synthesis. The average diameters

186 estimated from both BET and TEM measurements are reported in Table 1 and correspond
187 well to each other.

188 The grain size is larger for nanoparticles synthesized under Ar rather than He envi-
189 ronment. Particularly, the diameter of Cu/TiO₂-Ar nanoparticles deduced from the TEM
190 analyses seems to be 1.9 times larger than its bare TiO₂-Ar reference. It seems that the
191 addition of copper element promotes the formation of larger particles. This observation
192 together with the highest rutile content observed in this sample confirms a higher syn-
193 thesis temperature for Cu/TiO₂-Ar.



206 w
207 magnification TEM images of annealed Cu/TiO₂-He NPs (a) and Cu/TiO₂-Ar NPs (b); insets refer
208 to associated size distribution histogram fitted with the normal function.

209 XRD analyses were performed on all the samples before and after annealing (Figure
210 S.3). The samples consist on a mixture of a major anatase phase with minor rutile phase
211 except for Cu/TiO₂-Ar (Table 1). ~~A higher rutile proportion is observed in powders elab-~~
212 ~~orated under Ar, in good agreement with a higher flame temperature during the synthe-~~
213 ~~sis.~~ Finally, XRD patterns do not reveal peaks associated to copper species, probably due
214 to small crystallite sizes and low Cu content.

215 UV-Visible DRS optical analyses (Figure S.4) permitted to reveal a band gap be-
216 tween 3.0 and 3.2 eV, in good agreement with anatase (3.2 eV) and rutile (3.0 eV) corre-
217 sponding ratios in the annealed nanoparticles.

219 3.1.3. Chemical analyses

220 The presence of copper was first confirmed by ICP-OES analysis (Table 1). Cu
221 loadings are consistent regarding the 2.0 wt% Cu content in the liquid precursors. Re-
222 garding the copper content, it is slightly higher 1.91 ± 0.04 wt% (Cu/TiO₂-Ar) vs $1.76 \pm$
223 0.04 wt% (Cu/TiO₂-He) when the argon atmosphere is used. The reaction temperature
224 appears higher when working under argon atmosphere compared to helium atmosphere.
225 This higher temperatures induces a a better decomposition of copper precursor in argon
226 atmosphere and therefore a slightly higher Cu content in the powder. ~~Thus, copper pre-~~
227 ~~cursor decomposition during laser pyrolysis seems to be more efficient under argon at-~~
228 ~~mosphere than under helium.~~

229 High-angle annular dark-field imaging (STEM-HAADF) coupled to EDS chemical
230 analysis was employed in order to evidence the presence as well as the repartition of Ti
231 and Cu elements within the analyzed samples. From the STEM-HAADF images illus-
232 trated in Figure 2 and Figure S.5, the presence of bright spots were detected on the sur-
233 face of Cu/TiO₂-Ar (Figure 2a,c). The corresponding STEM-HAADF EDS map recorded
234 by considering the Cu K α edge illustrated in Figure 2b suggests that these bright spots
235 within the Cu/TiO₂-Ar powders are Cu-based nanoparticles localized within the whole
236 TiO₂ support. From the images we deduce that the size of these NPs is of $1.8 \text{ nm} \pm 0.3 \text{ nm}$
237 (Figure S.6). Moreover, STEM-HAADF EDS line scan analyses performed across the yel-
238 low line Cu/TiO₂-Ar (Figure 2c,d) confirm the presence of Cu species into 4 distinct NPs.

239 Moreover, these Cu NPs appear localized at the surface of TiO₂. On the contrary,
240 STEM-HAADF analyses performed on Cu/TiO₂-He sample (Figure 2e,f) do not show any
241 defined bright spot. The inset on corresponding EDS-Cu elemental map associated to
242 Cu/TiO₂-He image (Figure 2f) highlights a very poor contrast between Cu element (in
243 black) and the background (in white). From this inset, it can be seen Cu well-dispersed
244 species across TiO₂ particles. The STEM-HAADF EDS line scan analysis performed along
245 the yellow arrow (Figure 2g,h) confirms that Cu element is homogeneously dispersed
246 within TiO₂ most likely due to the lower specific surface area of TiO₂ nanoparticles when
247 synthesized under He. From this type of analysis we can sustain that there are significant
248 differences in terms of Cu dispersion and size within the TiO₂ support depending on the
249 materials synthesis conditions, i.e. the atmosphere in the present case.

250 XPS analyses were conducted to investigate the surface chemical state of elements in
251 both TiO₂ and Cu_xO_y/TiO₂ synthesized under different atmospheres. Figure S.7 depicts
252 the XPS full spectra of pure TiO₂ and Cu/TiO₂ which shows the presence of, Ti, O and C
253 for all samples. In addition, Cu element appeared in both Cu/TiO₂-He and Cu/TiO₂-Ar
254 powders. Ti 2p core level spectrum of TiO₂ (Table 2 and Figure S.8a,b) consists of two
255 peaks centered at 464.2 and 458.5 eV, corresponding respectively to Ti 2p_{1/2} and Ti 2p_{3/2} of
256 Ti⁴⁺ [18]. A broadening of Ti 2p doublet is observed for Cu_xO_y/TiO₂ samples in compari-
257 son to TiO₂ references (Table 2). Indeed, Ti 2p_{3/2} FWHM corresponds to 1.1 eV for both
258 TiO₂-He and TiO₂-Ar, and increases to 1.3 eV and 1.5 eV for Cu/TiO₂-He and Cu/TiO₂-Ar
259 samples, respectively. This suggests an interaction between copper species and TiO₂
260 through the incorporation of Cu ions in TiO₂ lattice [19,20].
261

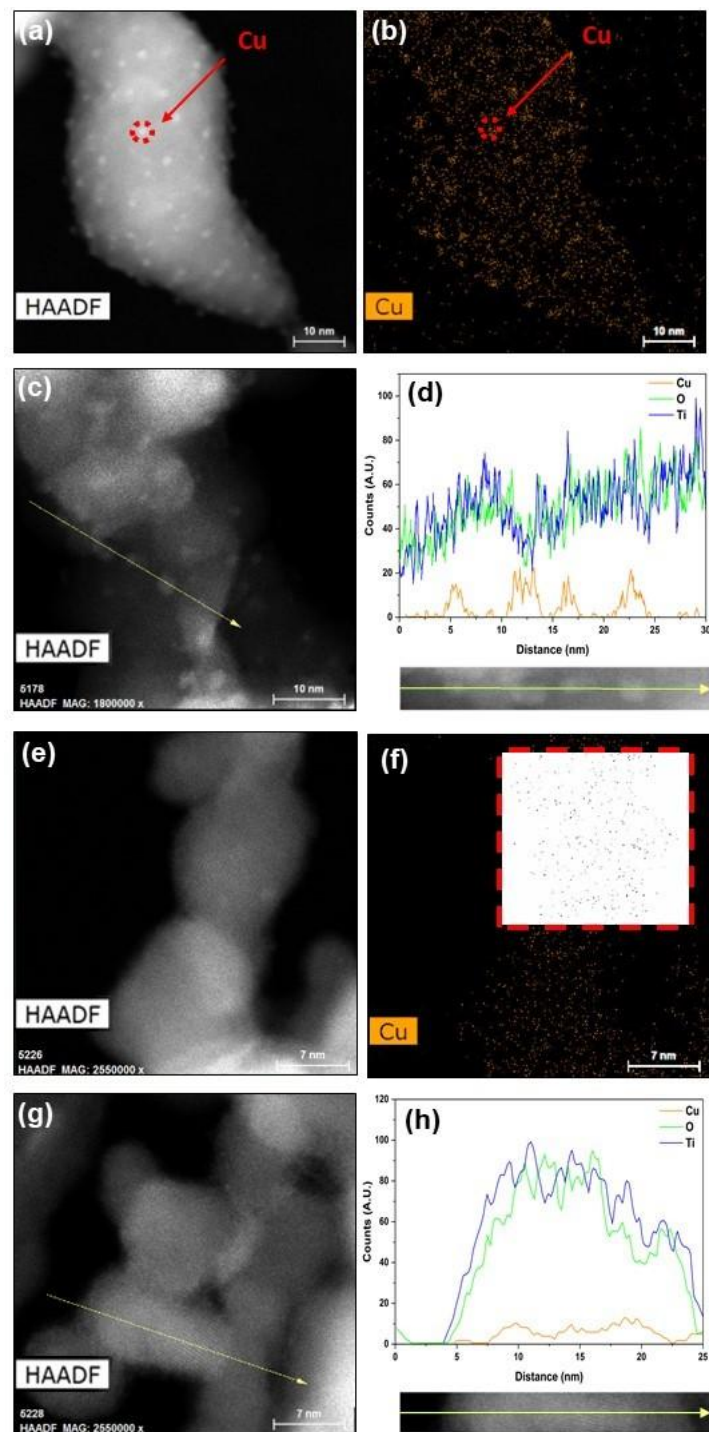


Figure 2. STEM-HAADF images and corresponding Cu elemental maps of Cu/TiO₂-Ar (a,b) and Cu/TiO₂-He (e,f) samples; STEM-HAADF images and associated EDS line scan analysis recorded along the yellow arrow performed on Cu/TiO₂-Ar (c,d) and Cu/TiO₂-He (g,h). Inset in (f) highlights the visualization of Cu element (black spots on white background) by the mean of a treatment operated on ImageJ software.

Cu 2p_{3/2} core-level spectrum (Figure 3) reveals several co-existing Cu chemical states in Cu/TiO₂-He and Cu/TiO₂-Ar [18,21]. The peaks at 934.8 eV and 933.2 eV are assigned to Cu²⁺ 2p_{3/2} signal, respectively Cu(OH)₂ and CuO. Shake-up satellite peaks confirm the presence of Cu²⁺. Besides, the component at about 932.5 eV refers to both Cu⁰ and Cu⁺ 2p_{3/2} signal, as the two oxidation states cannot be distinguished, having very close binding energies. By comparing Cu²⁺ proportions, it seems that copper species are more re-

262

263

264

265

266

267

268

269

270

271

272

273

duced in Cu/TiO₂-He sample. XPS quantification reveals copper content of 4.1 wt% and 9.2 wt% for Cu/TiO₂-He and Cu/TiO₂-Ar, respectively. It is 2.3 and 4.9 times higher than bulk values provided by ICP-OES analyses confirming a significant segregation of copper species on the surface of TiO₂, clearly pronounced in the case of Cu/TiO₂-Ar sample. In addition, Cu/Ti ratio is lower for Cu/TiO₂-He which could be attributed to a higher dispersion on the support [22,23] confirming our previous results.

Samples	Ti 2p _{3/2} (eV) [18]		Cu 2p _{3/2} (eV) [18,21]		Cu ²⁺ (at%)	Cu/Ti
	BE	FWHM	Cu ⁰ + Cu ⁺	Cu ²⁺		
TiO ₂ -He	458.5	1.1	-	-	-	-
Cu/TiO ₂ -He	458.5	1.3	932.5	933.3 ; 934.9	36.7	0.06
TiO ₂ -Ar	458.5	1.1	-	-	-	-
Cu/TiO ₂ -Ar	458.5	1.5	932.4	933.1 ; 934.7	49.3	0.14

Table 2. XPS analysis of TiO₂ and

Cu_xO_y/TiO₂ elaborated under He and Ar atmospheres.

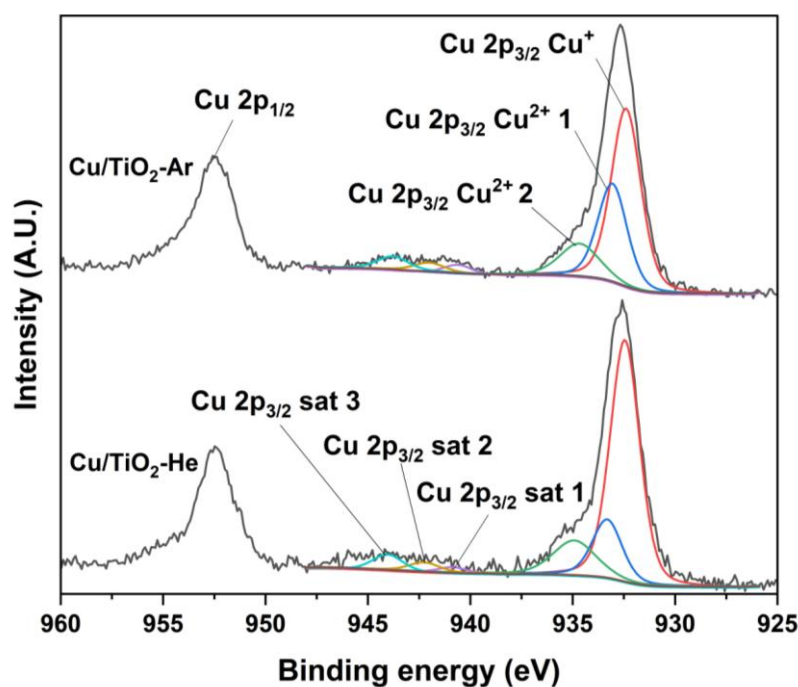


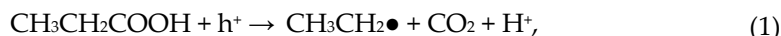
Figure 3. Cu 2p core-level spectra comparison of Cu/TiO₂-He and Cu/TiO₂-Ar samples.

Finally, the TiO₂ and Cu_xO_y/TiO₂ nanoparticles obtained by laser pyrolysis exhibit distinct morphologies: the Cu/TiO₂-He sample consists of nanoparticles of 10 nm range including very well dispersed Cu species on TiO₂, whereas Cu/TiO₂-Ar particles are about 30 nm with defined copper-based nanoparticles of about 2 nm size on TiO₂ support.

3.2. Photocatalytic PA degradation in anaerobic media

The main gases photoproducted from PA degradation under anaerobic conditions, presented in Figure 4 and a typical chromatogram is shown in Figure S.10. The identified gases are CO₂, ethylene C₂H₄, ethane C₂H₆ and H₂. Butane C₄H₁₀ (Figure S.9) was detected as a minor product. The principal mechanisms for saturated carboxylic acids degradation in oxygen-free media with pure TiO₂ or decorated with noble metals have already been

reported [11,13]. The first step consists on the decarboxylation of the carboxylic acid through the reaction with photo-generated trapped holes (Eq.1):



$\text{CH}_3\text{CH}_2\bullet$ radical can react with a $\text{H}\bullet$ ($\text{H}^+ + \text{e}^-$) to further form C_2H_6 in majority. Coupling of two $\text{CH}_3\text{CH}_2\bullet$ is responsible of C_4H_{10} formation, and two $\text{H}\bullet$ can form H_2 . According to Scandura *et al* [10], traces of ethylene are formed by the reaction of $\text{CH}_3\text{CH}_2\bullet$ with h^+ . Hence, from Eq.1, selectivities are defined in terms of hydrocarbon (C_2H_4 , C_2H_6) to CO_2 ratio.

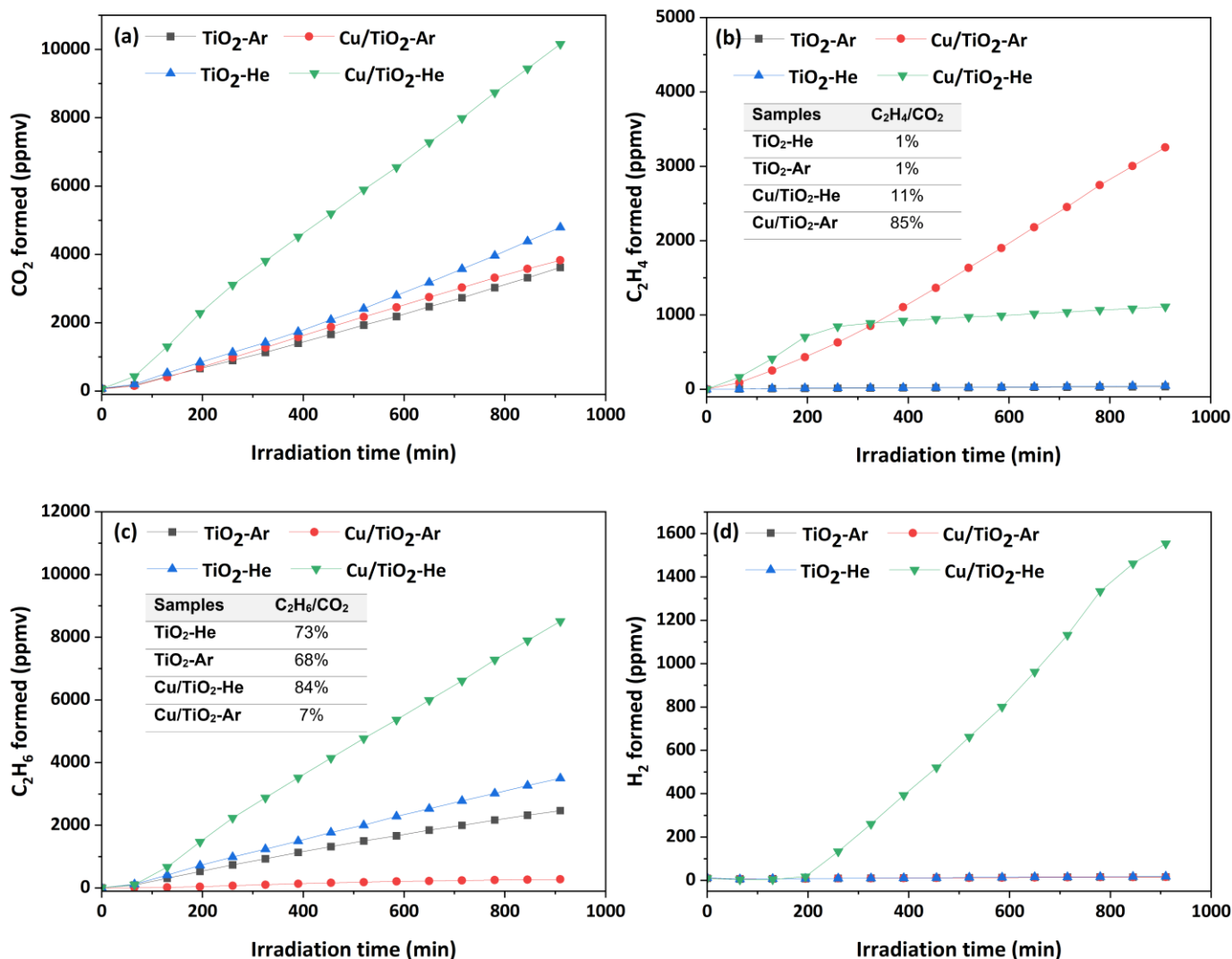


Figure 4. Major products formed from the photo-decarboxylation of PA (1 vol%) under UVA light: CO_2 (a), C_2H_4 (b), C_2H_6 (c), H_2 (d). Ratios are calculated at 910 min of irradiation.

Several differences can be seen from Figure 4. With pristine TiO_2 (black and blue curves, Figure 4), the main products are CO_2 and C_2H_6 ($\text{C}_2\text{H}_6/\text{CO}_2 = 73\%$ and 68% resp. for $\text{TiO}_2\text{-He}$ and $\text{TiO}_2\text{-Ar}$). The slight gain in photoactivity of $\text{TiO}_2\text{-He}$ observed in CO_2 and C_2H_6 productions could be attributed to its higher specific surface area compared to $\text{TiO}_2\text{-Ar}$ (111 vs $81 \text{ m}^2\cdot\text{g}^{-1}$) and/or to its higher anatase phase percentage. H_2 and C_2H_4 ($\text{C}_2\text{H}_4/\text{CO}_2 = 1\%$) are identified in trace amounts, in agreement with literature in absence of co-catalysts for H_2 [24–26] or with the use of noble metals (Pt, Au) for C_2H_4 [10–12].

Surface modifications on TiO_2 photocatalysts with copper/copper oxides lead to drastic changes in terms of levels of photo-generated products. Notably, $\text{Cu/TiO}_2\text{-He}$

318 appears as the most efficient photocatalyst for CO₂, C₂H₆ and C₄H₁₀ production (Figure
319 S.9) with C₂H₆ as the major hydrocarbon (green curve, Figure 4). C₂H₄ formation is en-
320 hanced (C₂H₄/CO₂ = 11%) till 200 min of reaction then it slows down. On the contrary H₂
321 production is increased from this same irradiation time (200 min). These phenomena
322 could be attributed to the efficiency of Cu_xO_y-TiO₂ heterojunction that decreases elec-
323 tron-hole recombination [27,28], but above all thanks to the reduction of copper oxides
324 into metallic copper [29–31]. Indeed, well dispersed copper species on TiO₂ surface in
325 Cu/TiO₂-He sample could be reduced after about 200 min of UV irradiation. Therefore,
326 Cu⁰, acting as an e⁻ scavenger, highly enhances H₂ formation. CH₃CH₂• radical preferen-
327 tially reacting with a H• formed on Cu⁰ site could explain how reduced copper species
328 inhibit the formation of C₂H₄ while enhancing C₂H₆ production.

329 Remarkably, Cu/TiO₂-Ar (red curve, Figure 4) is the most efficient material for C₂H₄
330 production: it is the major hydrocarbon product with a C₂H₄/CO₂ ratio in the range =
331 85-88%. Its formation evolves linearly at 260 ppmv/h, 130 times greater than the produc-
332 tion rate reached from pure titania. This efficient production is obtained at the expense of
333 C₂H₆ (C₂H₆/CO₂ = 4-7%) and H₂ formation. This contrasting behavior compared to
334 Cu/TiO₂-He may be related to less-dispersed, larger and oxidized copper nanoparticles
335 on TiO₂ support as seen by STEM-HAADF/EDS and XPS characterizations. The larger
336 size allows Cu_xO_y NPs resisting to complete photo-reduction as reported by Imizcoz *et al*
337 [29]. Besides, according to Yu *et al* [27], a larger Cu_xO_y size limits the direct transfer of
338 electrons from Cu_xO_y to H⁺ due to a decrease of conduction band. Consequently, H₂ and
339 C₂H₆ formations are not favored. These particular conditions seem to enhance C₂H₄
340 production as observed in the present study.
341

342 4. Conclusions

343 This study reports for the first time the significant production of C₂H₄ molecule from
344 photocatalytic degradation of propionic acid. TiO₂ nanoparticles modified with Cu_xO_y
345 used as photocatalysts were prepared by the laser pyrolysis synthesis method. The at-
346 mosphere of synthesis (argon or helium) strongly modifies Cu_xO_y/TiO₂ morphologies as
347 well as their photocatalytic properties. Cu_xO_y/TiO₂ obtained under helium consist on
348 small TiO₂ nanoparticles with highly-dispersed copper species which could be reduced
349 into Cu⁰ under UV irradiation. These reduced species promote the formation of H₂ and
350 C₂H₆ at the expense of C₂H₄. On the contrary, larger Cu_xO_y/TiO₂ NPs are obtained under
351 argon atmosphere with defined Cu_xO_y nanoparticles (1-2 nm diameter) on the surface of
352 TiO₂. It seems that such less-dispersed Cu_xO_y nanoparticles inhibit H₂ and C₂H₆ for-
353 mation. The major hydrocarbon is C₂H₄, with an outstanding selectivity higher than 85%
354 and outperforming by 130 times the ethylene production from pristine TiO₂. Although
355 the ethylene formation mechanism should be further examined, this study paves the way
356 to a new energy-saving way to produce C₂H₄ from organic acid without noble met-
357 al-based photocatalysts.

358 **Supplementary Materials:** The following supporting information can be downloaded at:
359 www.mdpi.com/xxx/s1, Figure S1: Images of TiO₂ and Cu/TiO₂ samples before (a) and after an-
360 nealing; Figure S2: TEM images and associated histograms of size distribution of TiO₂ powders.
361 Diameter measurements were performed on 100 particles with ImageJ software; Figure S3: XRD
362 patterns of Cu/TiO₂ samples before and after annealing (a); TiO₂ and associated Cu/TiO₂ samples
363 after annealing (b); XRD patterns of TiO₂ and Cu/TiO₂ as formed (c); Figure S4: Optical gap deter-
364 mination from UV-vis diffuse reflectance spectra using modified Kubelka-Munk function consid-
365 ering indirect gap of TiO₂; Figure S5: HAADF-STEM and Ti, O, Cu elemental maps performed on
366 Cu/TiO₂-Ar (a) and Cu/TiO₂-He (b); Figure S6: Histograms of size distribution of Cu nanoparticles
367 in Cu/TiO₂-Ar. Diameter measures were realized on 40 particles with ImageJ software; Figure S7:
368 XPS survey spectra of synthesized TiO₂ and Cu/TiO₂; Figure S8: Ti 2p (a,b), O 1s (c,d) and C 1s (e,f)
369 core-level spectra of synthesized TiO₂ and Cu/TiO₂; Figure S9: C₄H₁₀ formation from PA (1 vol%)
370 photo-decarboxylation under UVA light. C₄H₁₀/CO₂ ratios are calculated at 910 min of irradiation.

Author Contributions: J.K., P.L. and N.H.B. performed synthesis of samples. J.K. and F.D. performed photocatalytic tests. D.D. obtained and analyzed XPS data. I.F. made STEM analysis. N.H.B. and C.G. were directing this study. All authors were involved in writing the manuscript. All authors have read and agreed to the published version of the manuscript.

Funding: This research received no external funding.

Data Availability Statement: The data that support the findings of this study are available from the authors on reasonable request.

Acknowledgments: STEM-HAADF/EDS chemical analyses have been performed in the frame of the French Government program of investment for the future (Programme d'Investissement d'Avenir - TEMPOS Equipex – ANR-10-EQPX-50, pole NanoTEM). The authors would also like to acknowledge the Centre Interdisciplinaire de Microscopie électronique de l'X (CIMEX).

Conflicts of Interest: The authors declare no conflict of interest.

References

1. Zhang, M.; Yu, Y. Dehydration of Ethanol to Ethylene. *Ind. Eng. Chem. Res.* **2013**, *52*, 9505–9514, doi:10.1021/ie401157c.
2. Zimmermann H, W.R. Ethylene. *Ullmann's Encycl. Ind. Chem. Weinheim Wiley-VCH*; **2000**.
3. Bai, P.T.; Rajmohan, K.S.; Prasad, P.S.S.; Srinath, S. *Oxidative Dehydrogenation of Ethane to Ethylene Over Metal Oxide Catalysts Using Carbon Dioxide*; Springer Singapore, 2019; ISBN 9789811332968.
4. Haribal, V.P.; Chen, Y.; Neal, L.; Li, F. Intensification of Ethylene Production from Naphtha via a Redox Oxy-Cracking Scheme: Process Simulations and Analysis. *Engineering* **2018**, *4*, 714–721, doi:10.1016/j.eng.2018.08.001.
5. Ren, T.; Patel, M.; Blok, K. Olefins from Conventional and Heavy Feedstocks: Energy Use in Steam Cracking and Alternative Processes. *Energy* **2006**, *31*, 425–451, doi:10.1016/j.energy.2005.04.001.
6. Palmisano, G.; Augugliaro, V.; Pagliaro, M.; Palmisano, L. Photocatalysis: A Promising Route for 21st Century Organic Chemistry. *Chem. Commun.* **2007**, 3425–3437, doi:10.1039/b700395c.
7. Zhang, H.; Li, M.M.J. Crafting an Active Center with a Local Charge Density Gradient to Facilitate Photocatalytic Ethylene Production from CO₂. *Curr. Opin. Green Sustain. Chem.* **2022**, *36*, 100646, doi:10.1016/j.cogsc.2022.100646.
8. Guillard, C. Photocatalytic Degradation of Butanoic Acid: Influence of Its Ionisation State on the Degradation Pathway: Comparison with O₃/UV Process. *J. Photochem. Photobiol. A Chem.* **2000**, *135*, 65–75, doi:10.1016/S1010-6030(00)00275-6.
9. Scandura, G.; Rodríguez, J.; Palmisano, G. Hydrogen and Propane Production From Butyric Acid Photoreforming Over Pt-TiO₂. *Front. Chem.* **2019**, *7*, 1–14, doi:10.3389/fchem.2019.00563.
10. Scandura, G.; Sajjad, M.; Singh, N.; Palmisano, G.; Rodríguez, J. On the Selectivity of Butyric Acid Photoreforming over Au/TiO₂ and Pt/TiO₂ by UV and Visible Radiation: A Combined Experimental and Theoretical Study. *Appl. Catal. A Gen.* **2021**, *624*, 118321, doi:10.1016/j.apcata.2021.118321.
11. Kraeutler, B.; Bard, A.J. Heterogeneous Photocatalytic Decomposition of Saturated Carboxylic Acids on TiO₂ Powder. Decarboxylative Route to Alkanes. *J. Am. Chem. Soc.* **1978**, *100*.
12. Betts, L.M.; Dappozze, F.; Guillard, C. Understanding the Photocatalytic Degradation by P25 TiO₂ of Acetic Acid and Propionic Acid in the Pursuit of Alkane Production. *Appl. Catal. A Gen.* **2018**, *554*, 35–43, doi:10.1016/j.apcata.2018.01.011.
13. Sakata, T.; Kawai, T.; Hashimoto, K. Heterogeneous Photocatalytic Reactions of Organic Acids and Water. New Reaction Paths besides the Photo-Kolbe Reaction. *J. Phys. Chem.* **1984**, *88*, 2344–2350, doi:10.1021/j150655a032.
14. Zhang, N.; Liu, S.; Fu, X.; Xu, Y.J. Synthesis of M@TiO₂ (M = Au, Pd, Pt) Core-Shell Nanocomposites with Tunable Photoreactivity. *J. Phys. Chem. C* **2011**, *115*, 9136–9145, doi:10.1021/jp2009989.
15. Chen, Y.; Zhang, X.; Chen, Y. Propionic Acid-Rich Fermentation (PARF) Production from Organic Wastes: A Review. *Bioresour. Technol.* **2021**, *339*, 125569, doi:10.1016/j.biortech.2021.125569.
16. Pignon, B.; Maskrot, H.; Ferreol, V.G.; Leconte, Y.; Coste, S.; Gervais, M.; Pouget, T.; Reynaud, C.; Tranchant, J.F.; Herlin-Boime, N. Versatility of Laser Pyrolysis Applied to the Synthesis of TiO₂ Nanoparticles - Application to UV

- 415 Attenuation. *Eur. J. Inorg. Chem.* **2008**, 883–889, doi:10.1002/ejic.200700990.
- 416 17. Spurr, R.A.; Myers, H. Quantitative Analysis of Anatase-Rutile Mixtures with an X-Ray Diffractometer. *Anal. Chem.* **1957**, *29*,
417 760–762, doi:10.1021/ac60125a006.
- 418 18. Biesinger, M.C.; Lau, L.W.M.; Gerson, A.R.; Smart, R.S.C. Resolving Surface Chemical States in XPS Analysis of First Row
419 Transition Metals, Oxides and Hydroxides: Sc, Ti, V, Cu and Zn. *Appl. Surf. Sci.* **2010**, *257*, 887–898,
420 doi:10.1016/j.apsusc.2010.07.086.
- 421 19. Valero, J.M.; Obregón, S.; Colón, G. Active Site Considerations on the Photocatalytic H₂ Evolution Performance of Cu-Doped
422 TiO₂ Obtained by Different Doping Methods. *ACS Catal.* **2014**, *4*, 3320–3329, doi:10.1021/cs500865y.
- 423 20. Pham, T.D.; Lee, B.K. Disinfection of Staphylococcus Aureus in Indoor Aerosols Using Cu-TiO₂ Deposited on Glass Fiber
424 under Visible Light Irradiation. *J. Photochem. Photobiol. A Chem.* **2015**, 307–308, 16–22, doi:10.1016/j.jphotochem.2015.04.002.
- 425 21. Liu, Z.; Zhou, C. Improved Photocatalytic Activity of Nano CuO-Incorporated TiO₂ Granules Prepared by Spray Drying. *Prog.*
426 *Nat. Sci. Mater. Int.* **2015**, *25*, 334–341, doi:10.1016/j.pnsc.2015.07.005.
- 427 22. Obregón, S.; Muñoz-Batista, M.J.; Fernández-García, M.; Kubacka, A.; Colón, G. Cu-TiO₂ Systems for the Photocatalytic H₂
428 Production: Influence of Structural and Surface Support Features. *Appl. Catal. B Environ.* **2015**, *179*, 468–478,
429 doi:10.1016/j.apcatb.2015.05.043.
- 430 23. Ilie, M.; Cojocar, B.; Parvulescu, V.I.; Garcia, H. Improving TiO₂ Activity in Photo-Production of Hydrogen from Sugar
431 Industry Wastewaters. *Int. J. Hydrogen Energy* **2011**, *36*, 15509–15518, doi:10.1016/j.ijhydene.2011.09.029.
- 432 24. Al-Azri, Z.H.N.; Chen, W.T.; Chan, A.; Jovic, V.; Ina, T.; Idriss, H.; Waterhouse, G.I.N. The Roles of Metal Co-Catalysts and
433 Reaction Media in Photocatalytic Hydrogen Production: Performance Evaluation of M/TiO₂ Photocatalysts (M = Pd, Pt, Au) in
434 Different Alcohol-Water Mixtures. *J. Catal.* **2015**, *329*, 355–367, doi:10.1016/j.jcat.2015.06.005.
- 435 25. Tran, P.D.; Xi, L.; Batabyal, S.K.; Wong, L.H.; Barber, J.; Chye Loo, J.S. Enhancing the Photocatalytic Efficiency of TiO₂
436 Nanopowders for H₂ Production by Using Non-Noble Transition Metal Co-Catalysts. *Phys. Chem. Chem. Phys.* **2012**, *14*,
437 11596–11599, doi:10.1039/c2cp41450c.
- 438 26. Lan, L.; Daly, H.; Jiao, Y.; Yan, Y.; Hardacre, C.; Fan, X. Comparative Study of the Effect of TiO₂ Support Composition and Pt
439 Loading on the Performance of Pt/TiO₂ Photocatalysts for Catalytic Photoreforming of Cellulose. *Int. J. Hydrogen Energy* **2021**,
440 *46*, 31054–31066, doi:10.1016/j.ijhydene.2021.06.043.
- 441 27. Yu, J.; Hai, Y.; Jaroniec, M. Photocatalytic Hydrogen Production over CuO-Modified Titania. *J. Colloid Interface Sci.* **2011**, *357*,
442 223–228, doi:10.1016/j.jcis.2011.01.101.
- 443 28. Li, L.; Xu, L.; Shi, W.; Guan, J. Facile Preparation and Size-Dependent Photocatalytic Activity of Cu₂O Nanocrystals Modified
444 Titania for Hydrogen Evolution. *Int. J. Hydrogen Energy* **2013**, *38*, 816–822, doi:10.1016/j.ijhydene.2012.10.064.
- 445 29. Imizcoz, M.; Puga, A. V. Optimising Hydrogen Production: Via Solar Acetic Acid Photoreforming on Cu/TiO₂. *Catal. Sci.*
446 *Technol.* **2019**, *9*, 1098–1102, doi:10.1039/c8cy02349b.
- 447 30. Christoforidis, K.C.; Fornasiero, P. Photocatalysis for Hydrogen Production and CO₂ Reduction: The Case of
448 Copper-Catalysts. *ChemCatChem* **2019**, *11*, 368–382, doi:10.1002/cctc.201801198.
- 449 31. Jung, M.; Scott, J.; Ng, Y.H.; Jiang, Y.; Amal, R. Impact of Cu Oxidation State on Photocatalytic H₂ Production by Cu/TiO₂.
450 *Proc. 2014 Int. Conf. Nanosci. Nanotechnology, ICONN 2014* **2014**, 4–6, doi:10.1109/ICONN.2014.6965246.
- 451